10

Gate controlled Particle-Wave duality in a single walled carbon nanotube hole-transistor

Takafumi Kamimura
National Institute of Advanced Industrial Science and Technology
Japan Society for the Promotion of Science
CREST-Japan Science and Technology Agency
Japan

Kazuhiko Matsumoto
ISIR, Osaka University
National Institute of Advanced Industrial Science and Technology
CREST-Japan Science and Technology Agency
Japan

1. Introduction

Various electrode materials for single-walled carbon nanotube (SWNT) transistors were investigated. Pd electrodes have been used for Ohmic contacts (Javey et al., 2003). Ti electrodes have been used for Schottky contacts for hole conduction (Heinze et al., 2002; Martel et al., 2001; Kamimura & Matsumoto, 2005), and Mg and Ca electrodes for electron conduction (Nosho et al., 2006). Moreover, in the case of sub-μm order channel length at low temperature, SWNT transistors with Ohmic contacts have shown resonant tunneling transistor (RTT) characteristics (Liang et al., 2001), which are also called as Fabry-Perot characteristics, and SWNT transistors with Schottky contacts have shown single-hole transistor (SHT) characteristics (Suzuki et al., 2001), in which the Schottky barriers act as tunneling barriers. Therefore, electrodes materials should be chosen to obtain the desired characteristics.

In this study, we succeeded in fabricating a multifunctional quantum transistor using the particle nature and wave nature of holes in SWNT. This transistor can operate as an RTT and also as an SHT. An RTT is a device that uses the wave nature of hole and an SHT uses the particle nature of hole in the SWNT. Both devices need tunneling barriers at both sides of the quantum island. The RTT needs strong coupling while the SHT needs weak coupling between the quantum island and the electrodes. Usually, these tunneling barriers are made from thin oxide layers, etc. Therefore, the thickness of the tunneling barriers and the coupling strength cannot normally be controlled in a given device. In the present device, however, the Schottky barriers act as the tunneling barriers between the SWNT quantum island and electrodes. Therefore, the thickness of the tunneling barriers and the coupling strength between the SWNT and electrodes can be controlled by the applied gate voltage V_G.

Moreover, a SWNT is a cylindrical material with a diameter of several nanometers. The small diameter makes it possible to detect an electrical field from even a single-charge. Moreover, by observing the relative energy difference between the conducting carrier and the single-charges to be measured, it is possible to define the potential energy of the single-charges to be measured. However, as described in many reports (Kim et al., 2003; Radosavljevic et al., 2002), SWNT electron devices show hysteresis characteristics in gate voltage-drain current characteristics. The hysteresis characteristics are caused by gate-voltage-dependent charge fluctuation, e.g., adsorption of water molecules around a SWNT (Kim et al., 2003), charging into insulator layer around a SWNT (Radosavljevic et al., 2002), and charging into amorphous carbon around a SWNT (Martel et al., 2001) By eliminating these origins of the hysteresis characteristics, the number of fluctuating charges becomes small and a single-charge can be detected by a SWNT multi-functional quantum transistor.

2. Materials and methods

2.1 Method

We have eliminated the three origins of the hysteresis characteristics of a SWNT field effect transistor mainly pointed out in current reports (Martel et al., 2001; Kim et al., 2003; Radosavljevic et al. 2002; Kamimura & Matsumoto, 2004). To burn out amorphous carbon, we annealed a SWNT at low temperature in oxidizable atmosphere (Kamimura & Matsumoto, et al., 2004). To reduce the number of adsorbed atmosphere molecules, we covered the channel with a silicon dioxide layer. To reduce the number of trap sites in the insulator, we reduced channel length to 73 nm. The SWNT multi-functional quantum transistor fabricated by the process mentioned above shows almost no hysteresis characteristics in the gate voltage rage from -40 to 40 V. Moreover, an abrupt discrete switching of the source-drain current is observed in the electrical measurements of the SWNT multi-functional quantum transistor at 7.3 K. These random telegraph signals (RTS) are attributed to charge fluctuating charge traps near the SWNT multi-functional quantum transistor conduction channel. The current-switching behavior associated with the occupation of individual electron traps is demonstrated and analyzed statistically.

2.2 Sample preparations

A schematic of the sample structure is shown in Fig. 1. SWNT was prepared as follows. An n^+-Si wafer with a thermally grown 300 nm thick oxide was used as a substrate. Layered Fe/Mo/Si (2 nm/20 nm/40 nm) catalysts were evaporated using an electron-beam evaporator under a vacuum of 10^{-6} Pa. These layered catalysts were patterned on the substrate using the conventional photo-lithography process. SWNT was grown by thermal chemical vapor deposition (CVD) using the mixed gases of hydrogen and argon-bubbled ethanol. After the growth of the SWNT, it was purified by burning out the amorphous carbon around the SWNT in an air atmosphere at a temperature of several hundred degrees Celsius (Kamimura and Matsumoto, 2004). Ti (30 nm) electrodes were deposited on the patterned catalysts as the source and drain, and on the back side of the n^+-Si substrate for the gate, using the electron-beam evaporator under a vacuum of 10^{-6} Pa. The distance (L) between the source and drain was 73 nm. Thus, a back gate type multi-functional quantum transistor with an SWNT channel was fabricated that had the functions of an RTT and an

SHT. The single-charge measurement was carried out with the structure that silicon dioxide layer is on the SWNT channel.

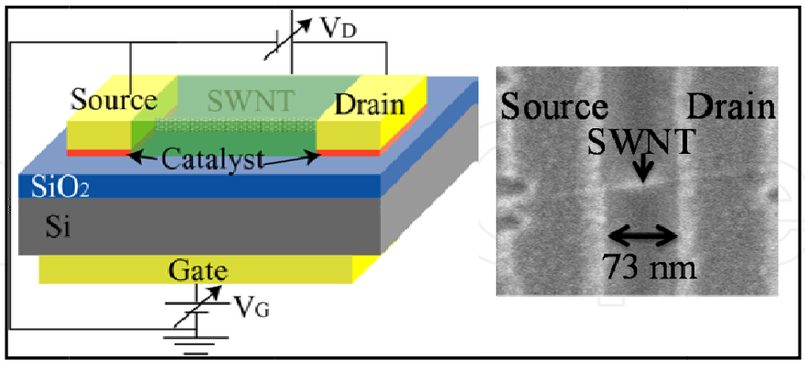

Fig. 1. Schematic structure of SWNT multi-functional quantum transistor covered by silicon dioxide layer. The channel length is 73 nm. The inset shows a SEM image around the channel before silicon dioxide deposition. A few charge storages are fabricated in the SiO_2 layer.

3. Results and discussions

3.1 Particle-Wave duality

Fig. 2(a) shows the differential conductance dI_D/dV_D characteristic as a function of the V_G at 7.3 K, where the drain voltage was set at 8 mV.

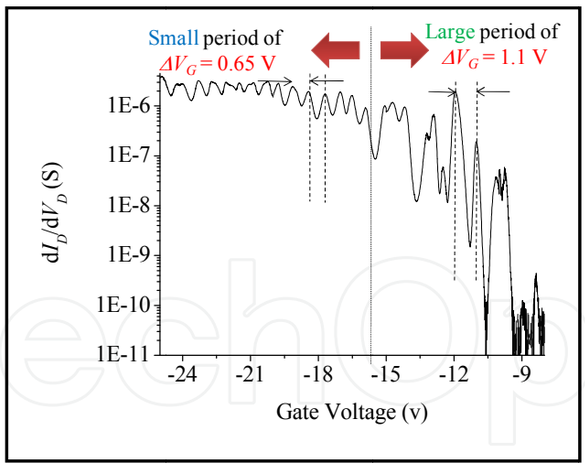

Fig. 2. (a) Differential conductance dI_D/dV_D characteristic as a function of V_G at 7.3 K. Two frequencies of oscillation were observed, which were ΔV_G = 1.1 V and 0.65 V.

An oscillation characteristic with two oscillation periods is also observed in Fig. 2(a). A large oscillation period of ΔV_G = 1.1 V was at $V_G \geq -16$ V and a small oscillation period of ΔV_G = 0.65 V was at $V_G \leq -16$ V. Fig. 2(b) shows the dI_D/dV_D peak on a linear scale at $V_G \geq -16$ V and $V_G \leq -16$ V. A clear difference in the oscillation period is observed as follows. The peaks of dI_D/dV_D at $V_G \geq -16$ V are well fitted by the Gaussian, i.e.

$$G \approx \frac{2e^2}{h}\frac{T_L T_R}{\Gamma}\frac{1}{2kT}exp\left(\frac{\varepsilon_F-\varepsilon_0}{2kT}\right), \quad (1)$$

and at $V_G \leq -16$ V by the Lorentzian, i.e.

$$G = \frac{2e^2}{h}\frac{4T_L T_R}{(\varepsilon_F-\varepsilon_0)^2+\Gamma^2} \quad (2)$$

as shown in Fig. 2(c) and (d), respectively, where e is the elementary charge, h is the plank constant, T_L and T_R are the tunneling probabilities at the left and right tunneling barriers, Γ is the full width at half maximum, k is the Boltzmann constant, T is the temperature, ε_F is the Fermi level, and ε_0 is the quantum level.

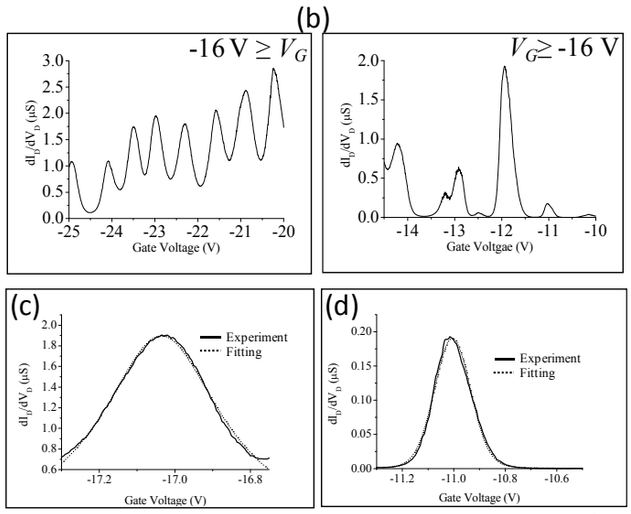

Fig. 2. (b) dI_D/dV_D peak in linear scale at low and high V_G. (c) dI_D/dV_D peak at V_G= -17 V (solid) and Lorentzian fitting line (dotted). The peak is well fitted by the Lorentzian function, which means the shape of the peak can be attributed to energy uncertainty broadening. Therefore, the peak must be a resonant tunneling current peak. (d) dI_D/dV_D peak at V_G = –11 V (solid) and Gaussian fitting line (dotted). The peak is well fitted by the Gaussian function, which means the shape of the peak can be attributed to thermal broadening. Therefore, the peak must be a Coulomb oscillation peak.

The shape of the Coulomb oscillation peaks must be Gaussian, which is attributed to thermal broadening, while the resonant tunneling current peaks must be Lorentzian, which is attributed to energy uncertainty (Radosavljevic et al., 2002). Therefore, the dI_D/dV_D oscillation at $V_G \geq -16$ V in Fig. 2(a) should be Coulomb oscillation peaks, and at $V_G \leq -16$ V in Fig. 2(a), they should be resonant tunneling current peaks. In other words, the device operates in particle nature mode at $V_G \geq -16$ V, and in wave nature mode at $V_G \leq -16$ V.
Fig. 3 shows the dI_D/dV_D characteristic as a function of the drain voltage V_D at 7.3 K and V_G = –12.795 V. The dI_D/dV_D peak spacing of 26 mV is observed in the plot, which corresponds to the quantum energy level separation in the SWNT quantum island. The separation of the quantum energy levels is indicated by

$$\Delta E_Q = \left(\frac{h\nu_F}{2L}\right)\left[1+\left(\frac{2L}{3rn}\right)^2\right]^{-\frac{1}{2}}, \tag{3}$$

where r is the radius of the SWNT, L is the length of the SWNT, and ν_F is the Fermi velocity (Kamimura & Matsumoto, 2004). When n becomes large, the equation becomes

$$\Delta E_Q = \frac{h\nu_F}{2L} \tag{4}$$

and shows a constant value independent of n.

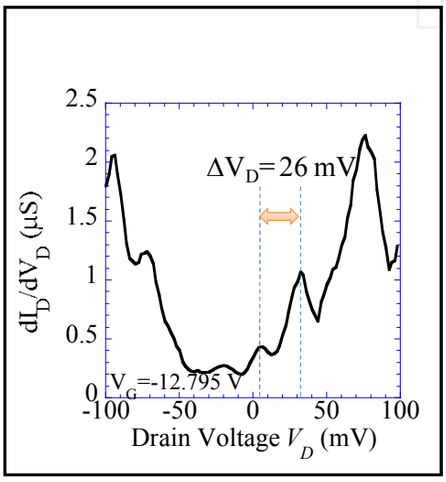

Fig. 3. dI_D/dV_D characteristic as a function of drain voltage V_D at V_G = –12.795 V and 7.3 K. The peaks are attributed to quantum energy levels in the SWNT. The estimated energy separation in 73 nm SWNT was 24 meV, which is in good agreement with the peak spacing of 26 mV in the plot.

The energy separation ΔE_Q of the quantum levels for an SWNT length of 73 nm is calculated to be 24 mV from eq. (2). Because this estimated value of energy separation of 24 mV is in good agreement with the dI_D/dV_D peak spacing of 26 mV in Fig. 3, it can be concluded that the entire SWNT channel acts as a single quantum island.

Fig. 4 shows a contour plot of the dI_D/dV_D characteristic as a function of V_G and V_D at 7.3 K. The characteristic can also be divided into two modes, the particle nature mode and wave nature mode. At $V_G \geq$ –16 V, as shown in Fig. 4(a) and (b), the plot clearly shows the Coulomb diamond structures, which are getting smaller with negatively increasing V_G. Additionally, line shaped quantum levels are observed outside of these Coulomb diamond structures. Therefore, at $V_G \geq$ –16 V, the device operated in the particle nature mode. As shown in Fig. 4(b), at –16 ≥ $V_G \geq$ –20 V, the Coulomb blockade was lifted and the Coulomb diamond structures disappeared at around V_G = –16 V. The quantum levels still remain and the so-called Fabry-Perrot quantum interference pattern is observed at this region. Finally, at $V_G \leq$ –20 V, the quantum levels are getting blurred with negatively increasing V_G, as shown in Fig. 4(c). Therefore, at –16 V ≥ V_G, the device operated in the wave nature mode.

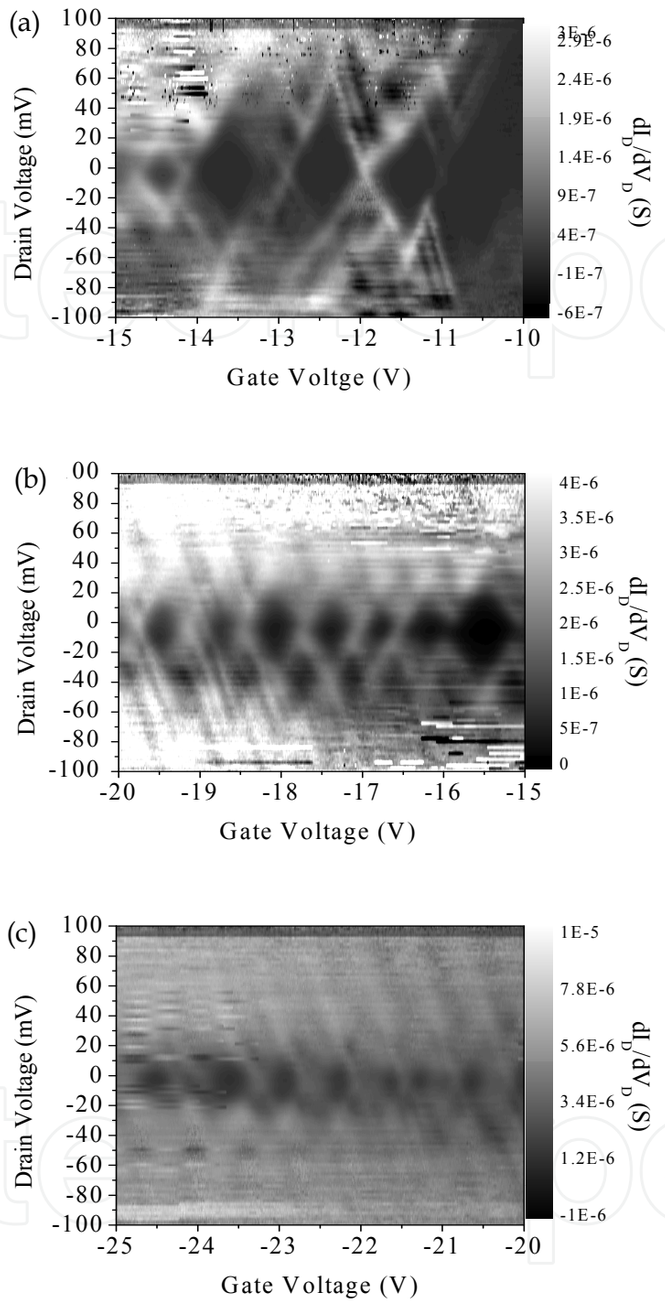

Fig. 4. Contour plot of dI_D/dV_D characteristic as a function of V_G and V_D at 7.3 K. (a) At $V_G \geq -16$ V, Coulomb diamond structures and line shaped quantum levels outside of the Coulomb diamond structures are observed. Moreover, the Coulomb diamonds become smaller with a negatively increasing V_G. (b) At $-16\ \text{V} \geq V_G \geq -20$ V, the Coulomb blockade is lifted and the Coulomb diamonds disappear. And the quantum levels become blurred with the negatively increasing V_G. The so-called Fabry-Perrot quantum interference pattern is observed. (c) At $-20\ \text{V} \geq V_G$, the blurred quantum levels still remain.

Fig. 5(a) shows the Coulomb charging energy E_C as a function of V_G. E_C is obtained by

$$E_C = \Delta E - E_Q \tag{5}$$

where ΔE is estimated from the size of the Coulomb diamond. E_C drastically decreases with a negatively increasing V_G, almost reaching zero at $V_G \geq -16$ V. Therefore, the Coulomb diamonds disappear at -16 V $\geq V_G$. Tunneling capacitance C_t and gate capacitance C_G as a function of V_G are shown in Fig. 5(b). C_t and C_G are obtained from

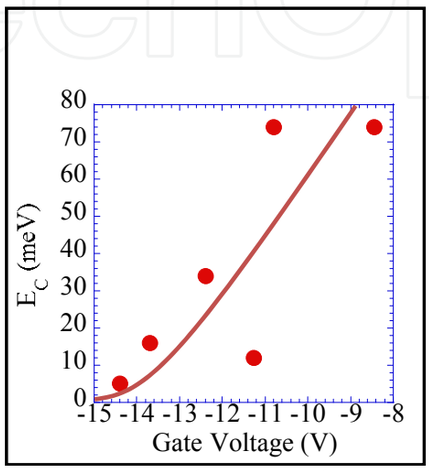

Fig. 5. (a) Coulomb charging energy E_C as a function of V_G. E_C drastically decreases at $V_G \geq -16$ V and reaches zero at around $V_G = -16$ V. Therefore, the Coulomb diamonds disappear at the mid-V_G region.

$$C_t = \mathrm{e}/2E_C - C_G \tag{6}$$

and

$$C_C = \mathrm{e}/\Delta V_G \tag{7}$$

respectively. C_t depends on the thickness of the tunneling barrier and C_G depends on the gate structure. C_t drastically increases with a negatively increasing V_G, while C_G is almost constant, independent of the changing V_G. The drastic increase in C_t is attributed to the decrease in the thickness of the Schottky barriers at the contacts between the SWNT quantum island and electrodes (Javey et al., 2003). When the Schottky barriers become thin with negatively increasing V_G, as shown in the inset of Fig. 5(b), C_t drastically increases and the coupling strength of the wave function between the outside and the inside of the Schottky barrier becomes stronger. Therefore, the Coulomb blockade is lifted and E_C becomes zero at -16 V$\geq V_G$.

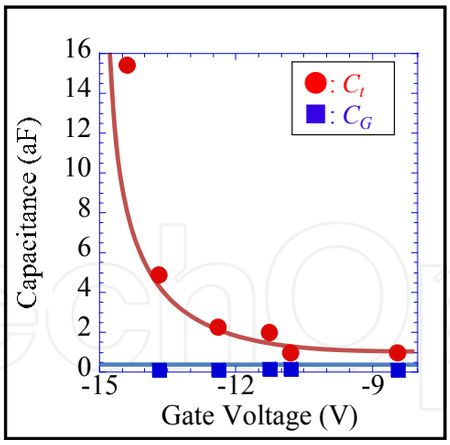

Fig. 5. (b) Tunneling capacitance C_t and gate capacitance C_G characteristics as functions of V_G. C_t drastically increases at $V_G \geq -16$ V. On the other hand, C_G is almost constant, independent of the changing V_G. The drastic increase of C_t is attributed to the change in the thickness of the Schottky barriers at the contact between the SWNT channel and electrodes.

The dependence of the full-width at half maximum (FWHM) of the resonant tunneling current peak characteristic on V_G is shown in Fig. 6(a).

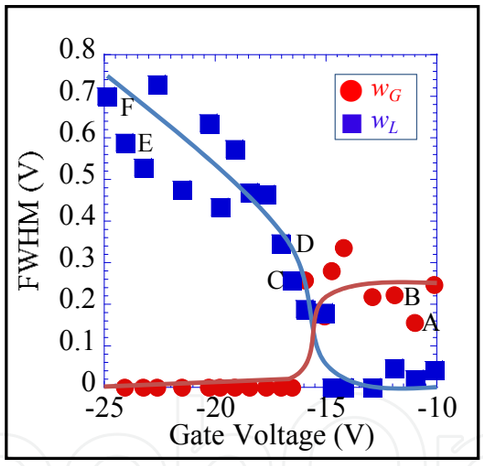

Fig. 6. (a) FWHM of the dI_D/dV_D peak characteristics as a function of V_G. w_G is almost constant, independent of V_G and w_L is negligibly small at $V_G \geq -16$ V. w_G become vanishingly small and w_L increases linearly with a negatively increasing V_G at -16 V $\geq V_G$.

The FWHM is estimated from an I_D-V_G plot using the Voigt function, which is a convolution of the Gaussian and Lorentzian functions, and can be used to divide the FWHM into the FWHM of the Gaussian w_G and that of the Lorentzian w_L. Fig. 6(b)–(d) shows several curves fitted by the Voigt function, where the solid line is the experimental data, the dotted lines are the fitting curves, the dashed line is the cumulative fitting curves, and each alphabetic marker for peaks A-F corresponds to a marker in the plot of Fig. 6(a).

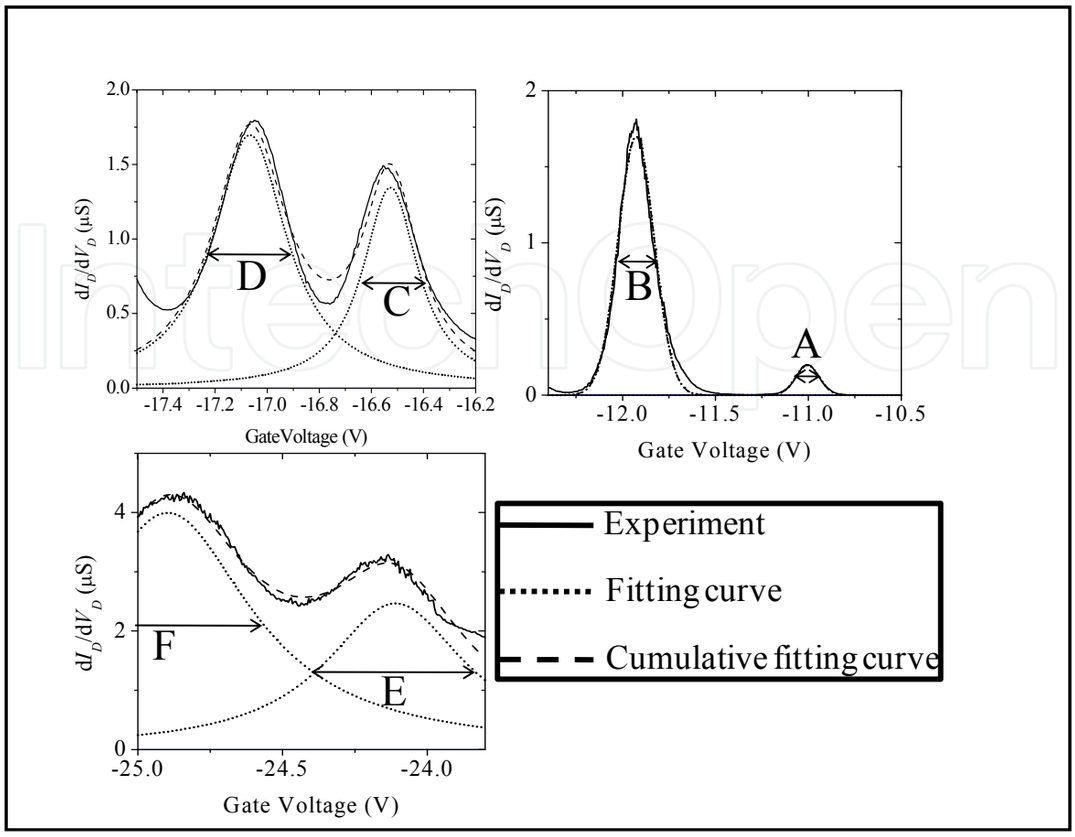

Fig. 6. (b)-(d) FWHMs: the experimental data are indicated by the black line, the fitting curves are indicated by the blue lines, the cumulative fitting curves are indicated by red line, and each alphabetic marker for a peak corresponds to a marker in the plot of Fig. 6(a).

In the particle nature mode of $V_G \geq -16$ V, w_L is negligibly small and the w_G of about 0.2 V is independent of V_G because the FWHM of the Coulomb oscillation mainly depends on the thermal broadening of Fermi dispersion (Foxman et al., 1993). On the other hand, in the wave nature mode of $-16\ \text{V} \geq V_G$, w_G becomes negligibly small and w_L increases linearly with the negatively increasing V_G. w_L is proportional to the tunneling probability as follows:

$$\alpha w_L = T\text{h}\nu_F/2L, \tag{8}$$

where α is the ratio of the modulated energy to applied V_G, and T is the tunneling probability (Kamimura & Matsumoto, 2006). Therefore, the increase in w_L seen in Fig. 6 represents an increase in the tunneling probability, which is attributed to the decrease in the thickness of the Schottky barriers with a negatively increasing V_G.

The logarithmic dependence of the drain current I_D on the inverse of the temperature is shown in Fig. 7.

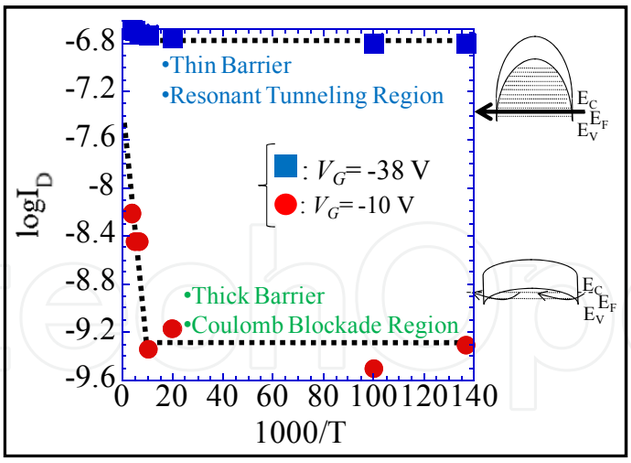

Fig. 7. The logarithmic dependence of the drain current I_D on the inverse of the temperature. At V_G = –38 V of the wave nature mode, I_D is almost constant, independent of the temperature. In the wave nature mode, the Schottky barrier is so thin that the tunneling current becomes dominant. In contrast, at V_G = –10 V of the particle nature mode, I_D drastically increases at the high temperature region, and the Schottky barrier height estimated from the slope is $\Delta\Phi$= 50 mV.

3.2 Hysteresis elimination

Fig. 8 shows the temperature dependence of differential conductance as a function of the gate voltage.

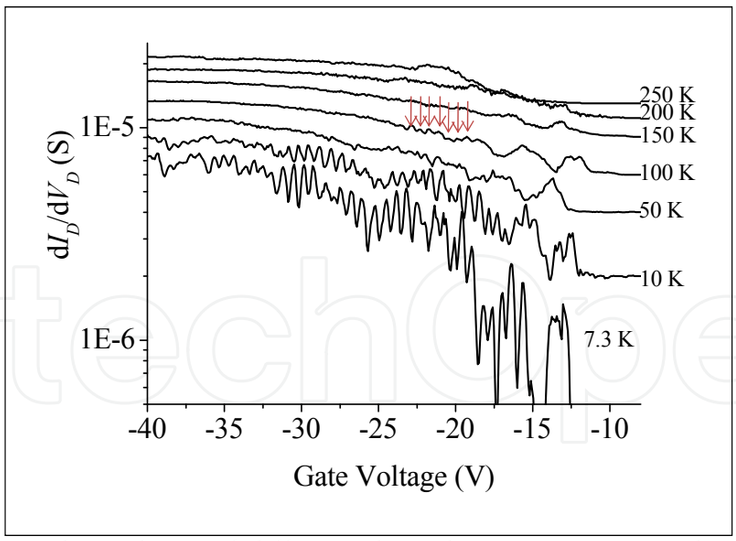

Fig. 8. Temperature dependence of differential conductance on V_G. Each plot is shifted by 3 μS to make it easier to see. The quantum level peaks are becoming blurred with increasing temperature. However, even at T = 100 K, the quantum levels remain, as indicated by the arrows.

The quantum levels peaks became blurred with increasing temperature. However, even at T = 100 K, the quantum levels still remained, as indicated by arrows.

The static characteristic measurement of the devise with silicon dioxide layer on the SWNT channel shown in Fig. 9 was carried out using an Agilent B 1500.

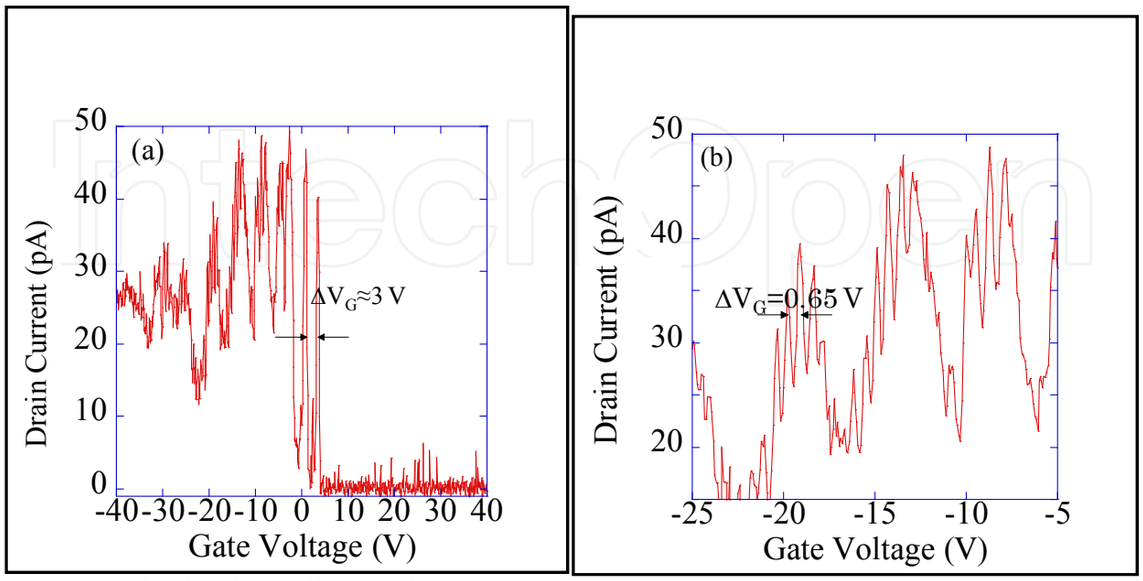

Fig. 9. (a) Coulomb oscillation characteristic at 7.3 K. Drain current was observed only in negative gate voltage regions, which indicates that the measured SWNT is a p-type semiconductor. A large period of ~3 V at an applied gate voltage of about V_G=0 V was observed, which was attributed to Coulomb oscillation characteristic. (b) The small period of ΔV_G=0.65 V of drain current peaks at 7.3 K, which was attributed to the quantum interference property, namely, Fabry-Perot interference of the hole, the coherent length of which was more than 73 nm. Coherent transport in the entire channel was achieved.

In the measurement, the data were integrated for a few seconds to eliminate the effect of noise, which was set by the equipment automatically. After that, the data were recorded. In the drain current I_D-gate voltage V_G characteristics of the SWNT multi-functional quantum transistor under a drain voltage of 11 mV at 7.3 K, the drain current showed a periodic peak- and valley structure with two periods. As shown in Fig. 9(a), I_D was observed only in the negative V_G region, which indicates that the measured SWNT was a p-type semiconductor. Moreover, a large period of ~3 V at around V_G=0 V was observed, which was attributed to the Coulomb oscillation characteristic. A part of Fig. 9(a) is expanded in the horizontal scale and shown in Fig. 9(b), where small period of ΔV_G=0.65 V was observed at a higher V_G, which was attributed to the Fabry-Perot interference property (Liang et al., 2001) of hole, the coherent length of which was more than 73 nm, and coherent transport in the entire channel was achieved. Fig. 9(c) shows a contour plot of the second-order differential conductance as a function of gate and drain voltages, in which a clear Fabry-Perot interference pattern can be seen.

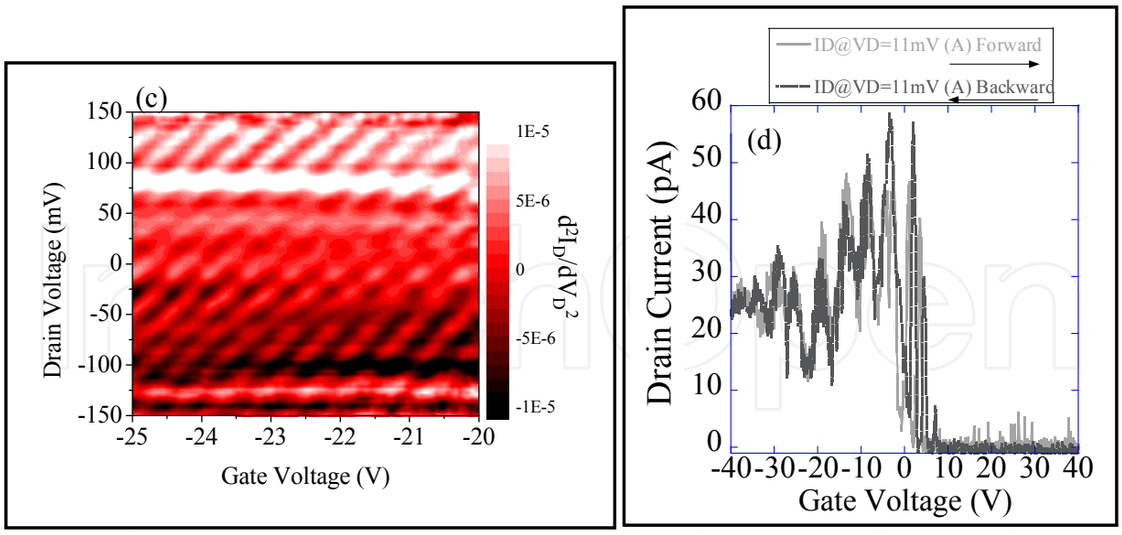

Fig. 9. (c) Contour plot of second-order differential conductance as a function of gate and drain voltages at 7.3 K, which shows a clear Fabry-Perot interference pattern. (d) Drain current-gate voltage characteristics with round trip applied gate voltage sweeping from V_G=40 to -40 V after sweeping from V_G=-40 to 40V at 7.3 K. The two drain current characteristics almost overlapped.

From the small period of drain current oscillation of ΔV_G=0.65 V and the equation (Kamimura & Matsumoto, 2006) of

$$\Delta E_Q = \alpha V_G = \mathrm{h}\nu_F/2L\mathrm{e}, \tag{9}$$

where ΔE_Q is the quantum energy separation, a is the gate modulation coefficient, h is Plank's constant, ν_F is the Fermi velocity in graphene, L is the length of the cavity of the hole, and e is the elementary charge, we estimated the width of the quantum well and obtained the length of the cavity of the hole L to be 55 nm. The estimated value is in agreement with the channel length 73 nm of the device which was obtained by scannig electron microscope (SEM) (inset of Fig. 1). The slight difference between the estimated L and the channel length must be attributed to the width of band bending in the SWNT e.g., Schottky barriers.

In Fig. 9(d), the gray (black) line shows drain current vs. applied gate voltage from -40 (40) to 40 (-40)V in a forward (backward) sweep of gate voltage. The SWNT multi-functional quantum transistor showed almost no hysteresis characteristics. The SWNT multi-functional quantum transistor was covered with a silicon dioxide layer, which prevents the SWNT from absorbing and releasing molecules in ambient, because fluctuation of molecules on the SWNT usually induces the hysteresis characteristics in the drain current-gate voltage characteristics. Moreover, the SWNT multi-functional quantum transistor has a small channel length of 73 nm, which reduced the number of trap sites near the SWNT and, at the same time, the number of trapped carriers causing hysteresis characteristics. We believe that the purification was effective to reduce the hysteresis characteristics. Thus, the hysteresis characteristic in the drain current–gate voltage characteristic was eliminated.

3.2 Single charge sensitivity of SWNT multi-functional quantum transistor

Figure 10(a) shows the time dependence of the conductance of the SWNT multi-functional quantum transistor at 7.3 K with a gate bias of V_G=-25.36 V. A short sampling time of 10 ms was set in the dynamic characteristic measurements shown in Fig. 10.

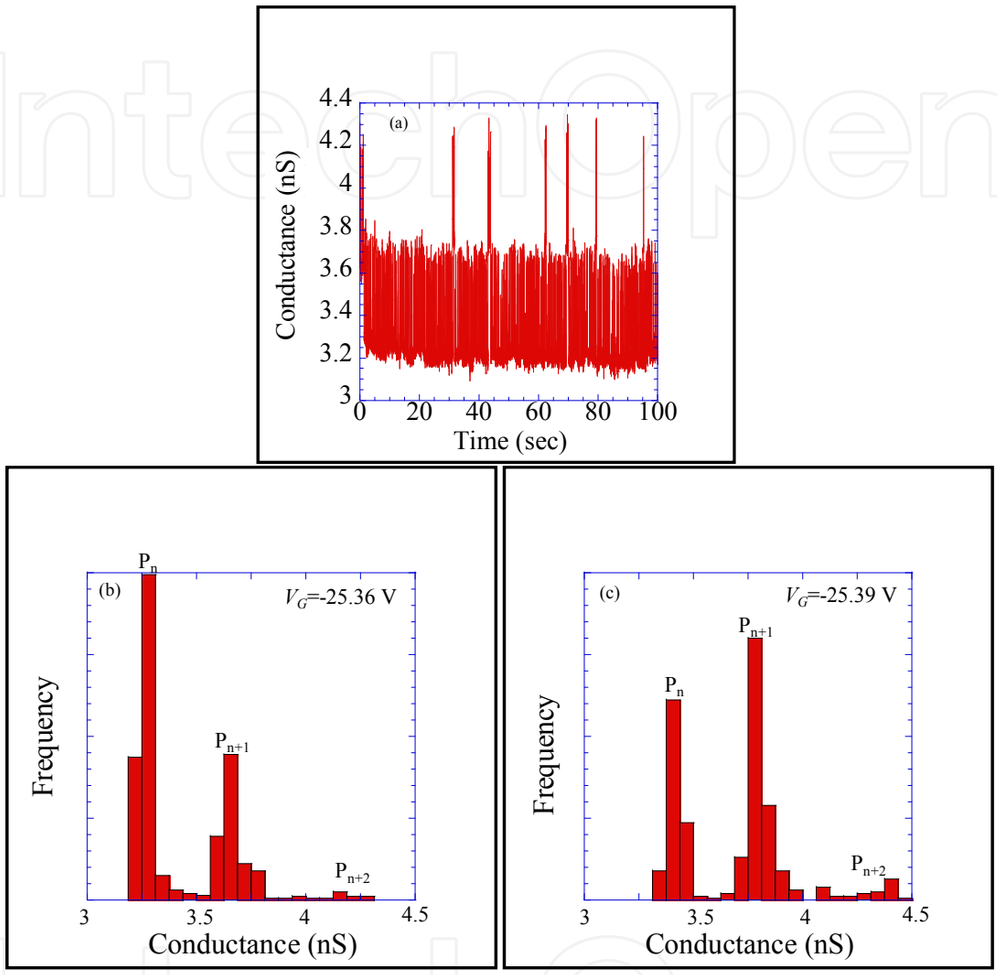

Fig. 10. (a) Time dependence of drain current with RTS at a gate voltage of V_G=-25.36 V. The time dependence of drain current was sampled for 100 s and the sampling time was 10 ms; (b) and (c) show histograms of the conductance levels of RTS at V_G= -25.36 and -25.39 V, respectively. P_n decreases and P_{n+1} and P_{n+2} increase with slightly increasing applied gate voltage from V_G= -25.36 to -25.39 V.

The applied gate voltage was under the Fabry-Perot interference region. The SWNT multi-functional quantum transistor shows RTS, as shown in Fig. 10(a), The RTS showed three levels, n, n+1 and n+2, of the conductance shown in Fig. 10(a). At a lower applied gate voltage, current levels higher than n+2 such as n+3 and n+4 appeared. The multiple levels of RTS are attributed to charge fluctuating charge storages near the conduction channels of the SWNT multi-functional quantum transistor. Moreover, because there was a single-charge storage including multiple energy levels or were some charge storages being at almost the same distances from the conductance channel of the SWNT multi-functional quantum

transistor, the RTS appeared. Figures 10(b) and 3(c) show histograms of the conductance levels of RTS at V_G= -25.36 V and V_G= -25.39 V, respectively. The three peaks of conductance of RTS expressed as P_n, P_{n+1}, and P_{n+2} are shown in Figs. 10(b) and 10(c). The conductance levels of the three peaks directly correspond to the conductance levels of RTS. On the other hand, the relative heights of the peaks correspond to occupation probabilities at each conductance level of the RTS. The heights of the peaks depend on applied gate voltage. P_n decreases and P_{n+1} and P_{n+2} increase with slightly increasing applied gate voltage from V_G= -25.36 to -25.39 V, which means that the energy levels in the charge storage are modulated by applied gate voltage.

The gate voltage dependences of the natural log of the ratio between the m_{th} peak and the $(m+1)_{th}$ peak in the conductance histogram P_{m+1}/P_m (m= n, n+1, n+2, ⋯, n+4) are shown in Fig. 11(a). The natural log of P_{m+1}/P_m linearly depends on applied gate voltage and saturates in each V_G. Each starting point of saturation is marked by an arrow in Fig. 11(a). The charge storage energy levels are floating. Therefore, modulations of energy by V_G may be different at each charge storage. We believe that the reason why the natural log of P_{m+1}/P_m saturates at each V_G may depend on the difference in energy modulation by V_G at each charge storage.

The charge transition is modeled, as shown in Fig. 12(a), in which the energy barrier is between the SWNT and the charge storage. Figures 11(b)-11(e) are enlargement plots of each P_{m+1}/P_m (m= n, n+1, n+2, ⋯, n+4). The energy differences ΔE_n between the charge storage energy level E_n and the Fermi level E_f are expressed as $\Delta E_n = E_f - E_n$, which is modulated by the applied gate voltage V_G. According to equilibrium statistical mechanics, P_{m+1}/P_m is given by (Peng et al., 2006)

$$P_{m+1}/P_m = \left(g_f/g_s\right)\mathrm{e}^{-\beta(E_f-E_n)} = \left(g_f/g_s\right)\mathrm{e}^{-\beta\Delta E_n} \tag{10}$$

where g_f and g_S are the degeneracy of the top of valence band and the charge storage, respectively. $g_f/\ g_S$ is assumed to be 1. β is 1/kT. E_n includes the contributions of e electrostatic potential induced by V_G, intrinsic energy level in the storage, and Coulomb charging energy. The basis of eq. (1) is the Arrhenius equation. In this model, the height of the barrier is the energy difference between E_f and E_n. Assuming a linear dependence of ΔE_n on V_G, ΔE_n can be written as $\Delta E_n = a e(V_0 - V_G)$, where a is the gate modulation coefficient, and is a constant value of 0.062. a is obtained from the periods of Fabry-Perot interference characteristic on V_D and V_G. V_0 is the offset voltage, and is obtained from the intersecting point of the extrapolating line of the fitting lines and the line of $\ln(P_{m+1}/P_m) = 0$. Therefore, eq. (1) is transformed to

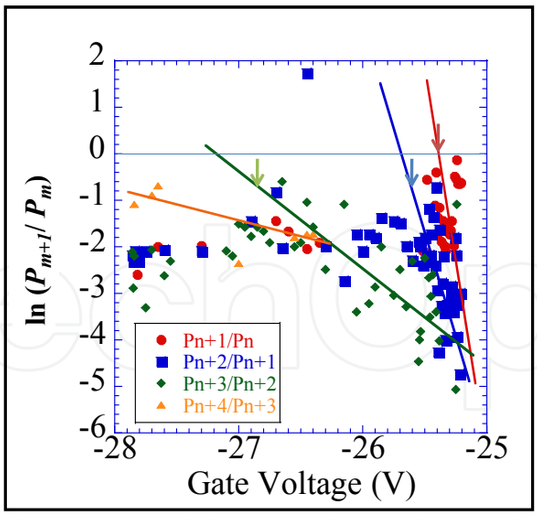

Fig. 11. (a) Gate voltage dependence of the natural log of the ratio between the occupancy probabilities of the mth current levels P_{n+1}/P_n.

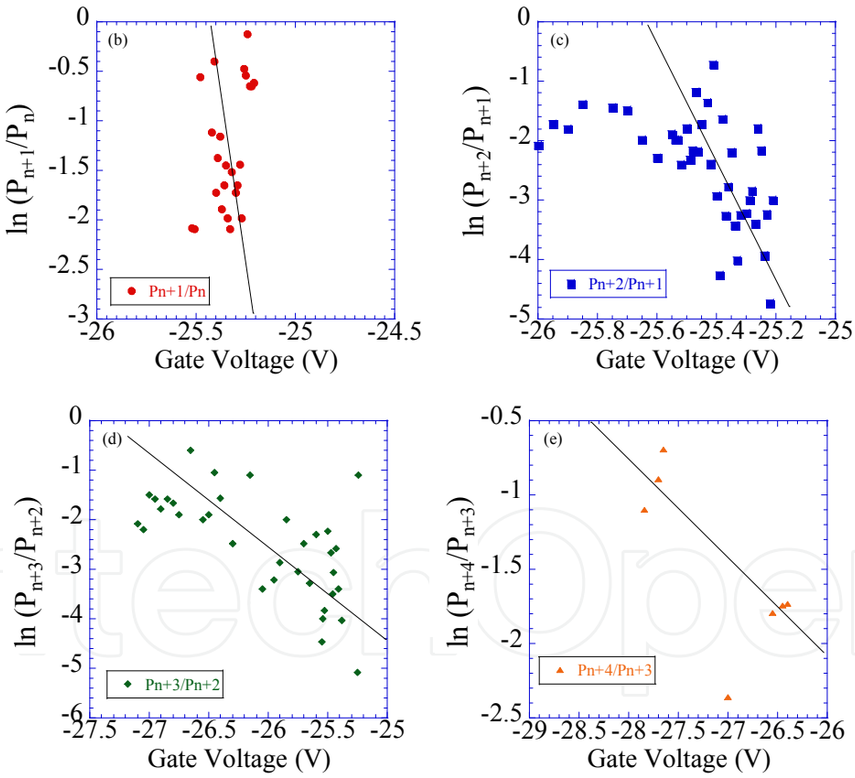

Fig. 11. (b)-(e) Enlargement plots of each P_{m+1}/P_m (m=n, n+1, n+2, ··n+4). The natural log of P_{n+1}/P_n was linearly dependent on gate voltage, the slopes of which are -10.4, -4.78, -1.47, and -0.690 V^{-1}, respectively.

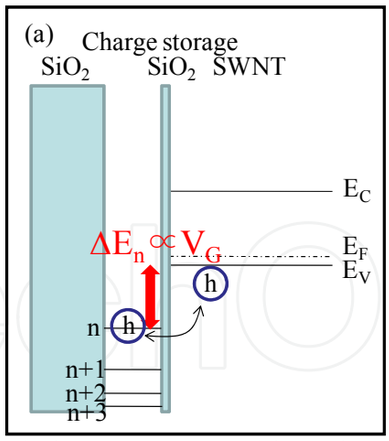

Fig. 12. (a) Schematic model of charge storage. When the charge storage energy level is coincident with the top of the valence band owing to applied gate voltage, the carrier goes and comes between them through the barrier with tunneling. The exiting probabilities of the carrier at the charge storage and the valence band depend on the relative height of their energy levels under equilibrium condition.

$$\ln(P_{m+1}/P_m) = -\beta e\alpha(V_0 - V_G) \tag{11}$$

Equation (2) is the transformed Arrhenius equation, in which V_G is the parameter.
From the dependence of P_{n+1}/P_n on V_G shown in Fig. 11 and eqs. (1) and (2), ΔE_n can be obtained, and is shown in Fig. 12(b). The obtained energy levels are from 1.57 to 1.79 eV.

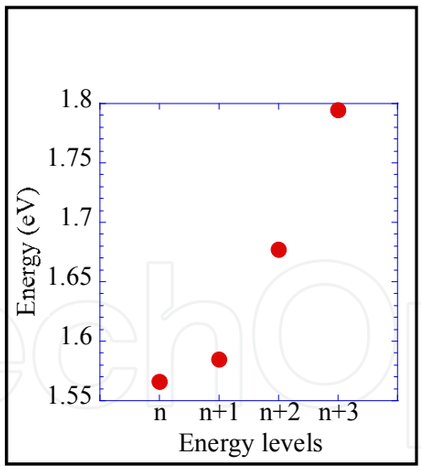

Fig. 12. (b) Estimated charge storage energy levels from the dependence of P_{n+1}/P_n on V_G shown in Figs. 4(b)-4(e) and eq. (1). The energy levels increase from 0.17 to 0.28 eV with increasing number of energy levels in the region of V_G from -25 to -28 V.

4. Conclusion

In summary, we succeeded in fabricating and demonstrating a multi-functional quantum transistor using the particle nature and wave nature of holes in SWNT. This transistor can

operate in the wave nature mode as an RTT and in the particle nature mode as an SHT. We were able to reveal that the principle of the characteristic transition from an SHT to an RTT is the modulation of the coupling strength between the SWNT quantum island and the electrodes by the applied V_G.

5. References

Foxman, E. B.; mcEuen, P. L.; Meirav, U.; Wingreen, Ned S.; Meir,Yigal; Belk, Paul A.; & Wind, S. J. (1993). Effects of quantum levels on transport through a Coulomb island. Phys. Rev., Vol. B 47, 10020-10023.

Heinze, S.; Tersoff, J.; Martel, R.; Derycke, V.; Appenzeller, J.; & Avouris, Ph. (2002). Carbon Nanotubes as Schottky Barrier Transistors. Phys. Rev. Lett., Vol. 89, 106801-1-106801-4.

Javey, A.; Guo, J.; Wang, Q.; Lundstrom, M. & Dai, H. (2003). Ballistic carbon nanotube field-effect transistors. Nature, Vol. 424, 654-657.

Kamimura, T. & Matsumoto, K. (2004). Reduction of Hysteresis Characteristics in Carbon Nanotube Field-Effect Transistors by Refining Process. IEICE Trans. Electron., Vol. E-87C, 1795-1798.

Kamimura, T. & Matsumoto, K. (2005). Electrical Heating Process for p-Type to n-Type Conversion of Carbon Nanotube Field Effect Transistors. Jpn. J. Appl. Phys., Vol. 44, 1603-1605.

Kamimura, T. & Matsumoto, K. (2006). Coherent Transport of Hole and Coulomb Blockade Phenomenon in Long p-Type Semiconductor Carbon Nanotube. Jpn. J. Appl. Phys., Vol. 45, 338-340.

Kim, W.; Javey, A.; Vermesh, O.; Wang, Q.; Li, Y.; & Dai, H. (2003). Hysteresis Caused by Water Molecules in Carbon Nanotube Field-Effect Transistors. Nano Lett., Vol. 3, 193-198.

Liang, W.; Bockrath, M.; Bozovic, D.; Hafner, J. H.; Tinkham, M. & Park, H. (2001). Fabry - Perot interference in a nanotube electron waveguide. Nature, Vol. 411, 665-669.

Martel, R.; Derycke, V.; Lavoie, C.; Appenzeller, J.; Chan, K. K.; Tersoff, J. & Avouris, Ph. (2001). Ambipolar Electrical Transport in Semiconducting Single-Wall Carbon Nanotubes. Phys. Rev. Lett., Vol. 87, 256805-1-256805-4.

Nosho,Y.; Ohno, Y.; Kishimoto, S. & Mizutani, T. (2006). Relation between conduction property and work function of contact metal in carbon nanotube field-effect transistors. Nanotechnology, Vol. 17, 3412-3415.

Peng, H. B.; Hughes, M. E. & Golovchenkoa, J. A. (2006). Room-temperature single charge sensitivity in carbon nanotube field-effect transistors. Appl. Phys. Lett., Vol. 89, 243502-243502-3.

Radosavljevic´, M.; Freitag, M.; Thadani,K. V. & Johnson, A. T. (2002). Nonvolatile Molecular Memory Elements Based on Ambipolar Nanotube Field Effect Transistors. Nano Lett., Vol. 2, 761-764.

Suzuki, M.; Ishibashi, K.; Ida, T.; Tsuya, D.; Toratani, K.; & Aoyagi, Y. (2001). Fabrication of single and coupled quantum dots in single-wall carbon nanotubes J. Vac. Sci. Technol., Vol. B 19, 2770-2774.

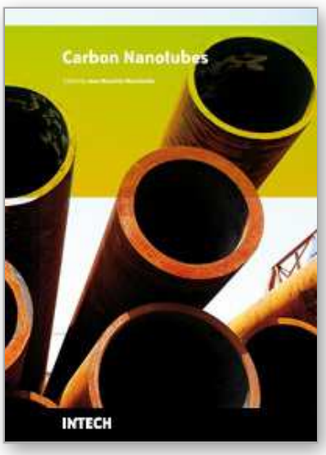

Carbon Nanotubes

Edited by Jose Mauricio Marulanda

ISBN 978-953-307-054-4
Hard cover, 766 pages
Publisher InTech
Published online 01, March, 2010
Published in print edition March, 2010

This book has been outlined as follows: A review on the literature and increasing research interests in the field of carbon nanotubes. Fabrication techniques followed by an analysis on the physical properties of carbon nanotubes. The device physics of implemented carbon nanotubes applications along with proposed models in an effort to describe their behavior in circuits and interconnects. And ultimately, the book pursues a significant amount of work in applications of carbon nanotubes in sensors, nanoparticles and nanostructures, and biotechnology. Readers of this book should have a strong background on physical electronics and semiconductor device physics. Philanthropists and readers with strong background in quantum transport physics and semiconductors materials could definitely benefit from the results presented in the chapters of this book. Especially, those with research interests in the areas of nanoparticles and nanotechnology.

InTech Europe
University Campus STeP Ri
Slavka Krautzeka 83/A
51000 Rijeka, Croatia
Phone: +385 (51) 770 447
Fax: +385 (51) 686 166
www.intechopen.com

InTech China
Unit 405, Office Block, Hotel Equatorial Shanghai
No.65, Yan An Road (West), Shanghai, 200040, China
中国上海市延安西路65号上海国际贵都大饭店办公楼405单元
Phone: +86-21-62489820
Fax: +86-21-62489821

IntechOpen